optica

Tailoring the potential landscape of room-temperature single-mode whispering gallery polariton condensate: supplementary material

HYUN GYU SONG, SUNGHAN CHOI, CHUNG HYUN PARK, SU-HYUN GONG, CHULWON LEE, MIN SIK KWON, DAE GWANG CHOI, KIE YOUNG WOO, AND YONG-HOON CHO*

Department of Physics and KI for the NanoCentury, Korea Advanced Institute of Science and Technology (KAIST), 291 Daehak-ro, Yuseong-gu, Daejeon 34141, South Korea
Corresponding author: yhc@kaist.ac.kr

This document provides supplementary information to "Tailoring the potential landscape of room-temperature single-mode whispering gallery polariton condensate," https://doi.org/10.1364/OPTICA.6.001313. It includes more details on (1) Materials and methods, (2) Hexagonal wire cavity system, (3) Hopfield coefficients for LP branches, (4) Polariton to photonic lasing transition, (5) Large Rabi splitting for room temperature polaritons, (6) Optical manipulation of polariton potential landscape, (7) Degree of polarization for polariton condensate, (8) Identification of mode via multiple slits interference, and (9) Tail fitting of Airy function.

1. MATERIALS AND METHODS

To grow GaN wires, n-type doped GaN film was grown on a sapphire substrate by metal-organic chemical vapor deposition (MOCVD), which is followed by a 50 nm SiO_2 mask layer deposition. Hole arrays of hexagonal pattern with a 1 μm diameter and a 3 μm pitch were opened on the mask layer by photolithography and dry etching process for selective area growth. Then undoped GaN wires were regrown on the hole opening arrays by MOCVD. GaN wires were mechanically dispersed with random orientation on a single crystal sapphire substrate for single-wire spectroscopy. To make a wire parallel or perpendicular to the monochromator slit, an attached rotational sample stage was utilized for alignment. A microscope objective lens with high N.A. (Zeiss, 150×, N.A.: 0.95) was used for excitation of the wire and collection of the emission in the normal direction. The diameter of the laser beam is varied from 200 nm to 5000 nm via the distance of the lens, f_2. A 3rd-harmonic Nd:YAG diode pumped solid-sate laser (CryLas, FQSS355-Q2) with a wavelength of 355 nm (pulse width: 1.1 ns, repetition: 10 kHz) and a 3rd-harmonic Ti-sapphire laser (Coherent, Chameleon Ultra II) with a wavelength of 266 nm (pulse width: 200 fs, repetition: 4 MHz) were used for optical excitation. μPL spectra were obtained using a monochromator (PI, IsoPlane-320) in combination with a 2D CCD detector (PI, PIXIS400) with a grating of 1800 grooves/mm. To measure a time decay profile of the excitons, a monochromator combining to a streak camera (Hamamatsu, C7700-01) was used for measuring wires at RT. To characterize a space-energy-resolved image, a real image from the objective lens was transferred to the 2D CCD of the monochromator using a 4-f system. To measure the momentum-energy dispersion curve of a polariton, a back-focal image (Fourier image) was formed using a 4-f system via the 1D confocal system to exclude emission from two end facets. The system's spatial resolution was ~ 133 nm, and its angular resolution was up to ~ 0.01 (sin θ).

2. HEXAGONAL WIRE CAVITY SYSTEM

For investigating the degree of photonic disorder in triangular-whispering gallery mode, we conducted confocal mapping of μPL spectra along the c-axis. The orientation of the wire is perpendicular to the slit direction of monochromator so that measured spectra is corresponding to the ground energy of each mode (i.e., θ_z=0). To identify photonic property, the linewidth of the lowest number mode, which was far from exciton energy level, has been investigated as shown in Fig. S1. Mean linewidth and fluctuation along the c-axis were 7.71 meV and ±0.69 meV, respectively. These values indicate at least three times lower

photonic disorder compared to those of nitride-based two-dimensional microcavity (4.66 meV and ±2.33 meV) [1]. This low photonic disorder is possible since the regular hexagonal shape, determined by the aspect ratio of mask opening shape, can be crystallographically sustained along c-axis. On the other hand, photonic energy linearly increases while Q-factor decreases along c-axis due to slightly tapered geometry of wire. The radius of the bottom part is 10 nm larger than the top part.
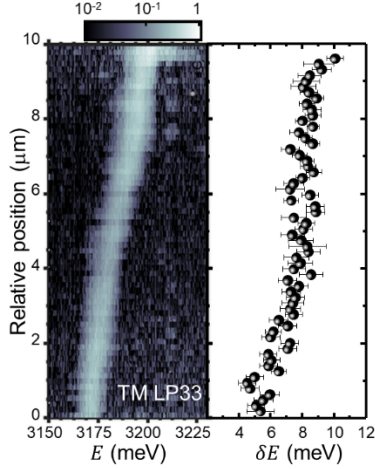

Fig. S1. Confocal mapping of μPL spectra for investigating photonic disorder (LP33). Confocal mapping of μPL spectra in logarithm scale (left). The x-axis for photon energy (E). Corresponding linewidth (δE) depending on the relative position (right).

We confocally measured angle-resolved μPL for two orthogonal detection angle (θ_z and θ_y) with a spatial filter to exclude the effect of two end facets (Fabry-Perot modes). The wire was rotated to set parallel or perpendicular to the slit of a monochromator for detection of E-θ_z and E-θ_y dispersion relation. As Fig. S2B shows, parabolic like dispersion along the z-axis (E-θ_z) indicates free motion of the electromagnetic field in this direction. On the other hand, the wave vectors in radial plane (x, y plane) are quantized with a discrete energy level (Fig. S2 (c)) [2], which shows horizontal dispersion relation. Multiple discrete states are revealed for detection θ_y due to two-dimensional optical confinement. In other words, electromagnetic modes are confined within the cross-section of the wire. Consequentially, we only consider two-dimensional confinement in hexagonal cross-section, i.e. triangular whispering gallery modes.
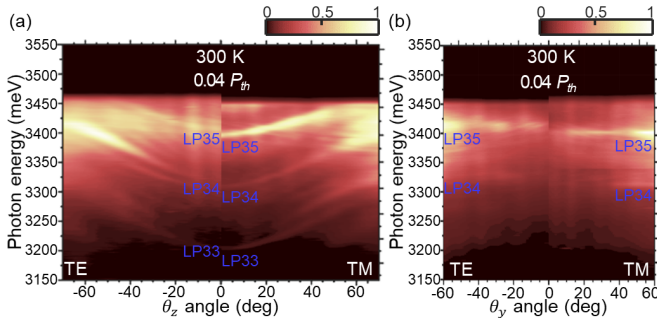

Fig. S2. Triangular whispering gallery modes as one-dimensional microcavity (a-b) Angle-resolved photoluminescence with detection angle θ_z (a), which is free motion axis, and θ_y (b) which is the confined axis.

3. HOPFIELD COEFFICIENTS FOR LP BRANCHES

We extracted photoluminescence spectra at around $\theta_z = 0$, corresponding to the ground state of polariton, from the angle-resolved photoluminescence as described in Fig. S3 (a). From the best fit of Lorentzian fitting, linewidth of LP containing higher mode number shows broader linewidth, as the polariton energy was closer to exciton energy level. This linewidth broadening was originated from exciton-phonon interaction [3] so that polariton with larger excitonic fraction represents broader linewidth. It shows clear behavior of polariton in contrast to the behavior of weak coupling regime [4].

Fig. S3 (b-d) represent the calculated Hopfield coefficients along θ_z for lower polariton mode number 33 (LP33), 34 (LP34), and 35 (LP35). The relative fraction of LP33 shows 0.03 for exciton and 0.97 for photon. Polariton lifetime was determined as the following relationship, $\tau_p^{-1}(k_z) = |C(k_z)|^2/\tau_c + |X(k_z)|^2/\tau_x$. The term related to exciton lifetime ($|X(k_z)|^2/\tau_x$) was about 5 orders smaller than the photon lifetime term ($|C(k_z)|^2/\tau_c$), so we concluded that LP33 corresponds to the photonic-like branch. By applying Fourier transform, τ_c deduced from the linewidth of photonic-like polariton branch was found to be 0.092 ps, which was quite similar to τ_c calculated from FDTD simulation (0.120 ps).
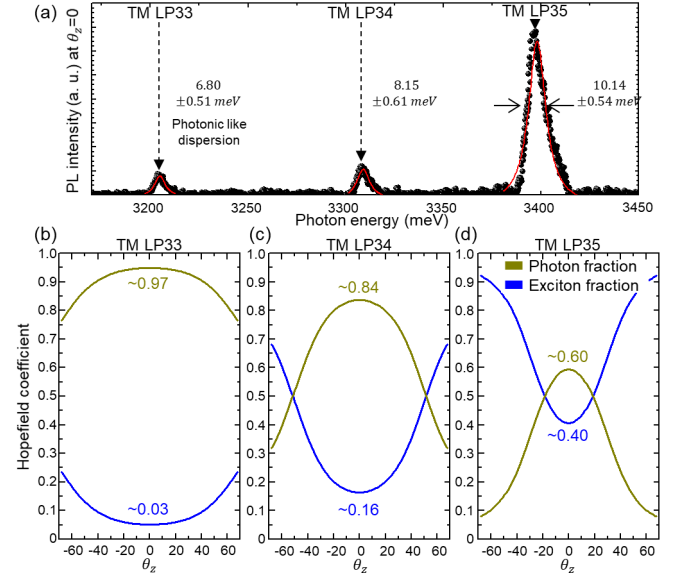

Fig. S3. Relative mixing fraction between excitons and photons. (a) Photoluminescence spectra at θ_z=0 from the angle-resolved photoluminescence. (b-d) Hopfield coefficients deduced from the angle-resolved photoluminescence for LP33-35. Blue solid lines for the fraction of excitons and yellow solid lines for the fraction of photons.

4. POLARITON TO PHOTONIC LASING TRANSITION

With the power density over 5.8 W/cm^2 (3.6 P_{th1}) corresponding to the second threshold power (P_{th2}), a new peak appeared at higher energy side with narrower linewidth compared to the polariton condensate as shown in the Fig. S4. (a). With further increase in the power density, peak shift shows redshift due to the bandgap renormalization effect and intensity of photonic lasing peak above the second threshold overwhelm the intensity of polaritons as shown in Fig. S4. (b), indicating the transition from strong-coupling to the weak-coupling regime. Calculated carrier density is $\sim 10^{18}$ cm^{-3} for this second threshold.
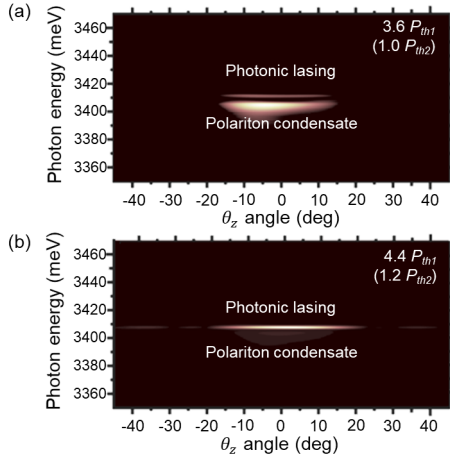
Fig. S4. Angle-resolved photoluminescence above the second threshold. (a) 3.6 P_{th1}, which is corresponding to P_{th2}. (b) 4.4 P_{th1}, which is corresponding to 1.2 P_{th2}.

5. LARGE RABI SPLITTING FOR ROOM TEMPERARTURE POLARITONS

Room temperature polaritons always confront LO-phonon scattering so that polariton branch has to be located quite lower energy side compared to exciton level to avoid LO-phonon scattering. There are two parameters to manipulate the energy of the polariton branch, one is detuning and the other is Rabi splitting energy. Thus, we quantitatively compare the lower polariton dispersions between LP1 (Rabi splitting energy 30 meV & detuning -77 meV), LP2 (Rabi splitting energy 90 meV & detuning -53 meV), and LP3 (Rabi splitting energy 150 meV & detuning -7 meV), which has the same ground state energy of polaritons. The polariton branch of small Rabi splitting with large detuning shows much steeper dispersion, which shows huge bottleneck effect, under the condition of same polariton energy of ground state ($\theta_z = 0$) as shown in the figure. In other hands, the dispersion of larger Rabi splitting with small detuning shows gradual dispersion, which reduces the bottleneck effect and induces efficient scattering with acoustic phonons to reach the ground state. Therefore, increasing Rabi splitting and reducing the detuning value is favorable for lowering the threshold at room temperature.
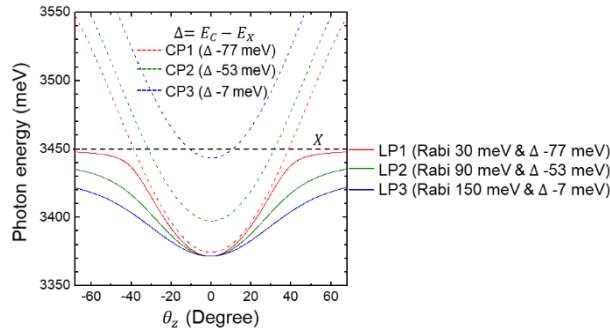

Fig. S5. Lower polariton branches under the condition of same ground state energy of polaritons in relation to Rabi splitting energy and detuning value.

6. OPTICAL MANIPULATION OF POLARITON POTENTIAL LANDSCAPE

To spatially manipulate the potential landscape of the tri-WG polariton condensates, we develop the optical setup to control the beam size of excitation as shown in Fig. S5. We intentionally adjust h of f_2 to give the effect of defocusing for excitation. The diameter of beam size can be continuously controlled from 200 nm to 5000

nm depending on h as measured in the inset of Fig. S4. It is worth noting that only the beam size of excitation part is variable, while the detection part from emission is invariant so that we can reliably measure data under the same detection condition.
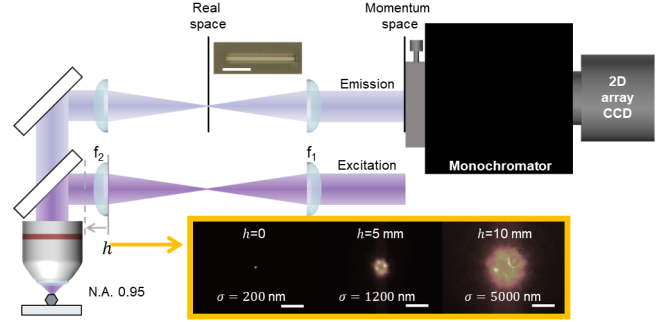

Fig. S6. Schematic of optical manipulation of polariton potential landscape. Laser beam size controlled by adjustment of the distance (h) of the lens (f_2) in the excitation part. The beam diameter varied from 200 nm to 5000 nm depending on h (inset). The scale bars in the inset represent 2 μm.

7. DEGREE OF POLARIZATION FOR POLARITON CONDENSATE

It is interesting to note that our first observation of GaN whispering gallery polariton condensate only exhibits TM polarization. This could be originated from the birefringent property. Birefringence of GaN [5, 6] shows ~0.05, which is ~3 times bigger compared to that of ZnO [7-10]. The extraordinary refractive index corresponding to TM mode had a higher refractive index compared to TE modes so that it can have larger Q-factor owing to effectively longer cavity distance. Thus, the whispering gallery polariton condensate only exhibits TM polarization with degree of polarization 0.92 at 1.0 P_{th} as shown in Fig. S6.
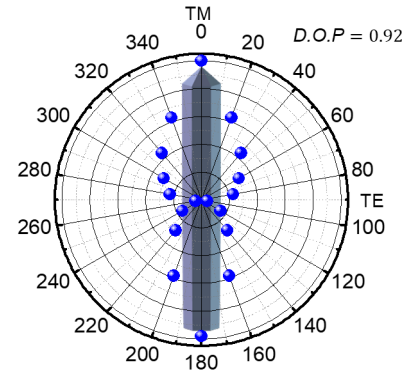

Fig. S7. Polarization dependence of the polariton condensate. Whispering gallery polariton condensate only exhibits TM polarization with a high degree of polarization (e.g., 0.92 at 1.0 P_{th1}).

8. IDENTIFICATION OF MODE VIA MULTIPLE SLITS INTERFERENCE

In general, WGMs can have two types of photonic modes in a hexagonal cavity. One is hexagonal and the other is triangular. To rigorously identify the generated photonic mode, we performed FDTD simulation with the configuration as shown in Fig. S7 (a). Two monitors are recorded for the electric field profile with TM polarization of the cross-section in the real-space and the momentum-space. In particular, the monitor for the momentum-space is located the half lambda distance above the top of the wire surface to exclude the near-field effect. Fig. S7 (b) and (c) is the electric field profile of hexagonal WGM without the substrate and

triangular WGM, respectively, from the real-space monitor. Corresponding momentum space images represent in Fig. S7 (d) and (e) from the momentum-space monitor. To identify the polariton mode, the momentum-space image was measured for observation of the interference pattern [11] generated by each corner of the hexagonal cross-section. The peculiar interference pattern along θ_y is attributed to the multiple-slits interference of the single-mode tri-WG polariton condensate, which yields the spatial coherence. These leakages, which are from four corners to the strong scattering, are analogous to the point-like sources going through the slits. The interference pattern along θ_y from our structure shown in Fig. 3 (b) is attributed to the multiple-slits interference of the tri-WG polariton condensate, which shows quite good agreement to the triangular WGM (Fig. S7 (e)) but not hexagonal WGM (Fig. S7 (d)). The real space image of the theses leakages is directly observed as shown in Fig. 5 (a). Since wires are dispersed on a sapphire substrate in our case, electric fields of both hexagonal-WGMs and inverted tri-WGMs leak out to the substrate due to interface between the substrate and the wire. Therefore, only upright tri-WGMs can dwell long time in the microcavity. Thus, we can rigorously identify the photonic mode formed in the hexagonal cavity by exploiting the spontaneously formed interference pattern.
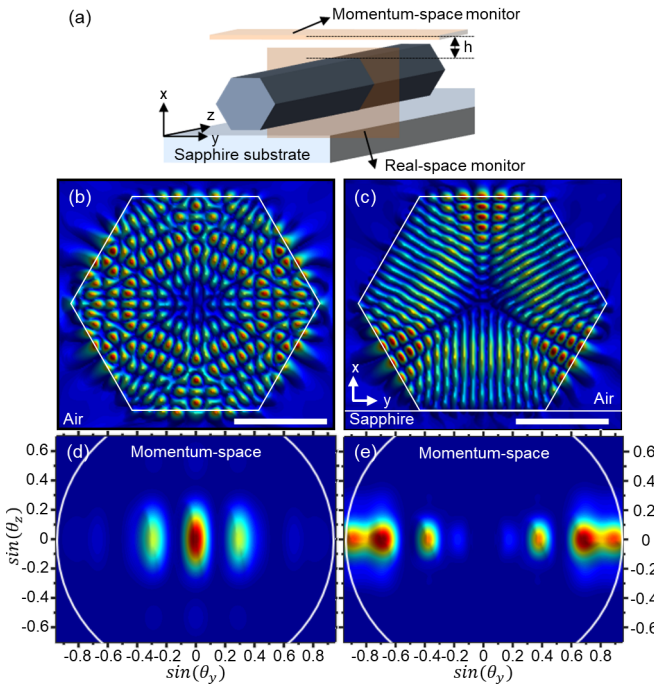

Fig. S8. Multiple slits interference pattern from the hexagonal cavity (a) Schematic of FDTD simulation. (b-c) Calculated electric field profile of a cross-section of a hexagonal cavity without the substrate (b) and with the substrate (c). (d-e) Momentum-space image of the hexagonal WGM (d) and the triangular WGM (e).

9. TAIL FITTING OF AIRY FUNCTION

To explore the disorder effect, we verified the correlation between momentum and real space. For information of real space, we applied the region far outside pump area [12] of Gross-Pitaevskii equation for our one-dimensional structure. Considering linear potential due to the tapered geometry, corresponding equation (Airy equation) can be expressed by

$$\frac{\hbar^2}{2m}\frac{\partial^2}{\partial z^2}\psi(z)+\left\{\hbar(\omega_c-\omega_0)+\frac{i\hbar}{2\tau_p}\right\}\psi(z)+\alpha z\psi(z)=0 \quad (S1)$$

τ_p is polariton lifetime. ω_c and ω_o were the energy for moving polariton state and ground state of polaritons, respectively. The corresponding solution is

$$I=|\psi(z)|^2=|c\times A_i(-(k_c^2+i\frac{k_c}{v_g\times\tau_p}+\frac{k_c^2}{\Delta E}\alpha z)/(-\frac{k_c^2}{\Delta E}\alpha z)^{2/3})|^2 \quad (S2)$$

where A_i is Airy function. $\hbar(\omega_c-\omega_0)$ and k_c were determined by ARPL and α was extracted from the line scan data (Fig. S1). The only fitting parameters are $v_g\times\tau_p$ and c. To apply the region of far outside the pump area, we conducted tail fitting for the area larger than FWHM of exciton reservoir as described in Fig. S7. For a top (bottom) graph of Fig. S6, it shows exponential-like (Gaussian-like) decay profile probably due to uphill road (downhill road) of potential.
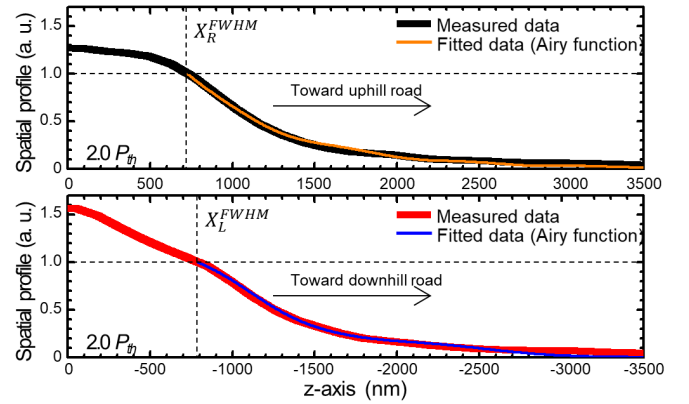

Fig. S9. Tail fitting of Airy function for one-dimensional polariton system. The measured spatial profile of extended polariton condensate (black solid lne) and the tail fitted result (yellow solid line) toward the uphill road of potential (top). The measured spatial profile (red solid line) and the tail fitting result (blue solid line) toward the downhill road of potential (bottom).

Reference

[1] G. Rossbach, J. Levrat, E. Feltin, J.-F. Carlin, R. Butté, and N. Grandjean, "Impact of saturation on the polariton renormalization in III-nitride based planar microcavities", Phys. Rev. B **88**, 165312 (2013).

[2] A. Trichet, L. Sun, G. Pavlovic, N. A. Gippius, G. Malpuech, W. Xie, Z. Chen, M. Richard, and L. S. Dang, "One-dimensional ZnO exciton polaritons with negligible thermal broadening at room temperature", Phys Rev B **83**, 041302 (2011)

[3] Trichet A, Médard F. Zúñiga-Pérez J, Alloing B, Richard M. "From strong to weak coupling regime in a single GaN microwire up to room temperature", New. J. Phys. **14**, 073004 (2012)

[4] T. Hu, W. Xie, L. Wu, Y. Wang, L. Zhang, Z. Chen, "Optimized polaritonic modes in whispering gallery microcavities", Solid State Commun. **262**, 7 (2017)

[5] S. Shokhovets, M. Himmerlich, L. Kirste, J. Leach, S. Krischok, "Birefringence and refractive indices of wurtzite GaN in the transparency range", Appl. Phys. Lett. **107**, 092104 (2015)

[6] G. E. Jellison, C. M. Rouleau, "Determination of optical birefringence by using off-axis transmission ellipsometry", Appl. Opt. **44**, 3153 (2005)

[7] J. Wang, W. Xie, L. Zhang, D. Xu, W. Liu, J. Lu, Y. Wang, J. Gu, Y. Chen, X. Shen, and Z. Chen, "Exciton-polariton condensate induced by evaporative cooling in a three-dimensionally confined microcavity", Phys. Rev. B **91**, 165423 (2015)

[8] D. Xu, W. Xie, W. Liu, J. Wang, L. Zhang, Y. Wang, S. Zhang, L. Sun, X. Shen, Z. Chen, "Polariton lasing in a ZnO microwire above 450 K", Appl. Phys. Lett. **104**, 082101 (2014)

[9] D. Xu, W. Xie, W. Liu, J. Wang, L. Zhang, Y. Wang, S. Zhang, L. Sun, X. Shen, Z. Chen, "Polariton lasing of quasi-whispering gallery modes in a ZnO microwire", Appl. Phys. Lett. **103**, 022103 (2013)

[10] W. Xie, H. Dong, S. Zhang, L. Sun, W. Zhou, Y. Ling, J. Lu, X. Shen, and Z. Chen, "Room-temperature polariton parametric scattering driven by a one-dimensional polariton condensate", Phys. Rev. Lett. **108**, 166401 (2012)

[11] D. Saxena, F. Wang, Q. Gao, S. Mokkapati, H. H. Tan, and C. Jagadish, "Mode Profiling of Semiconductor Nanowire Lasers"**,** Nano Lett. **15**, 5342 (2015)

[12] M. Wouters, I. Carusotto, and C. Ciuti, "Spatial and spectral shape of inhomogeneous nonequilibrium exciton-polariton condensates", Phys. Rev. B **77**, 115340 (2008).